7 Alternative Ignition Systems

7.1 Transient Plasma Ignition (TPI) for Automotive Applications

Sayan Biswas, Isaac Ekoto, Riccardo Scarcelli

Abstract

Transient plasma ignition (TPI) – where high-energy, non-equilibrium plasma ignites flammable mixtures – has been found to promote faster flame propagation rates through a combination of larger volume ignition kernels and the generation of active radicals that enhance flame speeds. For the present study, ignition and early flame propagation characteristics of TPI were investigated within a custom-built optically accessible spark calorimeter for near-atmospheric stoichiometric mixtures of propane and air. Transient plasma was generated using an available high-voltage (~ 25 kV peak), short duration (~12 nanosecond) pulse generator. Two electrode configurations were investigated: (1) a wide-gap pin-to-pin and (2) a groundless partial dielectric barrier discharge (DBD) igniter with a flush mounted and exposed anode tip. Each electrode was expected to promote faster initial burn rates through some combination of reduced heat transfer losses, formation of radical species favorable for ignition, and distributed ignition sites within the combustion chamber. Important post-discharge products were bulk-sampled from non-flammable fuel/air mixtures and speciated via gas chromatography. The impact of the post-discharge products on the flame speeds and auto-ignition delay times were evaluated using the 0-D combustion commercial solver CHEMKIN PRO. High-speed schlieren imaging was used to characterize discharge streamer phenomena and flame propagation rates. Flame propagation measurements were benchmarked against a similar operating point that used a high-energy inductor coil spark plug (93 mJ).

For transient plasma discharges in air, the pin-to-pin electrodes generated strong twin streamers that bridged the electrode gap. Complementary discharge modeling indicates elevated electron densities and atomic oxygen concentrations, especially around the anode tip. Conversely, air discharge imaging of excited state atomic oxygen for the groundless partial DBD igniter indicates strong negative corona streamers that propagate up along the insulator surface toward the expose anode. Corresponding post-discharge sampling and speciation via gas chromatography reveals substantial dissociation of parent fuel molecules into smaller hydrocarbon constituents. Complementary CHEMKIN PRO modeling indicates these species will increase laminar flame by up to 20%. Finally, it was found that both the pin-to-pin and groundless partial DBD igniters increased flame propagation rates by a factor of 2 relative to the inductor coil spark igniter due to a combination of reduced electrode heat losses, larger ignition volumes, and the formation of radicals that increase initial flames speeds.

1. Introduction

The aggressive move of modern spark-ignited (SI) gasoline engines towards challenging dilute and boosted combustion regimes necessitate new and robust ignition devices. Heavy charge dilution by exhaust gas recirculation (EGR) or air can improve fuel efficiency and lower engine-out pollutant emissions [1]. Benefits include (1) reduced throttling losses, (2) lower heat transfer losses and (3) low nitrogen oxide (NOx) and particulate (PM) emissions [2]. However, reduced flame propagation speeds at relative comparable stoichiometric conditions result in combustion stability issues.

Transient Plasma Ignition (TPI) is a promising advanced ignition technology that utilizes short pulse (~10s of nanoseconds), high-voltage (15 kV+) electrical discharges to generate highly energized low-temperature plasma (LTP). Conventional inductor coil spark plugs utilize point-based thermal plasmas that have electron energies in equilibrium with the bulk-gas energy but have fallen out of favor due to poor tolerance to dilution by air or exhaust-gas recirculation [3]. Conversely, LTP ignition has gained increased attention as a way to promote the formation of radical species favorable for combustion. Broadly speaking, plasma-assisted ignition systems sorted by increasing reduced electric field strength (i.e., electric field strength, E, normalized by the gas number density, N) include: microwaves [4, 5], radio-frequency resonant discharges [6, 7], and transient plasma discharges [8, 9].

The major benefit of transient plasma over other LTP technologies is the higher E/N that leads to increased ionization and dissociation rates due to limited collisional electron energy transfer effects [10]. Fast voltage rise-times can result in E/N values greater than 100 Townsend with electron energies above 10 electron volts, while the short pulse widths enable modest discharge energies (10s of mJ) [11, 12]. Transient plasma discharges have been used to extend dilution tolerance limits through the formation of active radicals that shorten ignition delays [13] and rapid volumetric heating via electron energy transfer processes [14-16]. Ignition has been observed to start from the electrode tips, with inhomogeneous propagation into the bulk gas [17, 18].

Previous studies have shown that TPI generates radicals and other electronically excited species over a relatively large volume [13-18]. However, fundamental TPI mechanisms – particularly at engine relevant conditions – remain poorly understood. In the present study, ignition and early flame propagation characteristics were investigated within a custom-built optically accessible spark calorimeter undergoing TPI. An available high-voltage (25 kV peak), short duration (~12 nanoseconds) pulse generator was used to generate transient plasma. Two different electrode configurations were tests: (1) an opposed pin-to-pin electrode and (2) a groundless partial dielectric barrier discharge (DBD) electrode. For the pin-to-pin configuration, faster initial burn rates are expected through the formation of distributed ignition sites and strong field concentrations at both the anode and cathode tips. Transition to breakdown is avoided through a combination of short pulse widths and large inter-electrode distances (5.2 mm). For the groundless partial DBD electrode, the anode is surrounded by approximately 1.5 mm of a dielectric alumina ceramic in the shape of a cone frustum, with the anode surface exposed and flush mounted with the ceramic tip. Ignition is expected to happen at the exposed anode, with significant enhancement of the flame speeds resulting from negative corona surface discharges that surround the

insulator. Flame propagation measurements were benchmarked against those from a similar operating point that used a high-energy inductor coil spark plug as the ignition source.

2. Experimental Approach

2.1. Ignition Testing Vessel

All experiments were performed in the stainless steel 316 custom-built, optically accessible, spark calorimeter illustrated in Figure 1 (a). The experimental apparatus has been discussed in detail by Wolk and Ekoto [19], with a brief summary presented here. The calorimeter has an internal volume of 29 cm^3. To visualize the TPI event, 3 optical UV grade quartz (Corning 7980) windows were installed in the calorimeter body. A 20 mm diameter front viewing window enabled direct imaging and fluorescence signal collection from the laser measurement. Two orthogonally installed side windows with 16 mm diameter clear apertures of 12.7 mm allowed for a pulsed light for schlieren imaging of the streamer volume and ignition kernel to pass through the chamber. The initial calorimeter temperature, $T_{initial}$, was heated to 70°°C using resistive heat tape connected to temperature controllers with the temperature monitored using embedded K-type thermocouples. The calorimeter was filled to the desired pressure (1.3 bar absolute) using fuel and desiccated air. Key specifications and operating conditions of the calorimeter are reported in Table 1.

Table 1: Calorimeter specifications and operating conditions.

Internal volume (cm^3)	29
Distance between electrodes (mm)	5.2 mm
Initial temperature (°C)	70
Initial pressure – speciation (bar)	1.1 – 6.1
Initial pressure – ignition (bar)	1.3
Voltage (kV)	10.3 – 25.0
Gas density (kg/m^3)	1.1 - 6.2
Oxidizer composition (% volume)	20.95% O_2, 78.08% N_2, 0.93% Ar, 0.04% CO_2
Fuel	C_3H_8
Purge and fill cycle time (s)	120

To generate the transient plasma discharges within the calorimeter, a Transient Plasma Systems Inc. SSPG-101-HF high-voltage (25 kV peak) pulse generator with a ~12-ns full width at half max (FWHM) pulse width and 5 ns rise time was used. A low-impedance inline attenuator probe was used to monitor pulse voltage and current for each discharge event. Two distinct types of electrodes were tested. For the opposed electrode configuration, the relative position of the anode and cathode is schematically shown in Figure 1 (b). The high-voltage anode was built by modifying an NGK DP7EA-9 size M12 non-resistor spark plug. The plug J-hook and top 1 cm of the outer body ground were removed, with the anode tip machined to a rounded point (~125 μm radius of curvature) to maximize local electric field strengths, while maintaining relatively repeatable discharge characteristics. The anode was centrally positioned at the top of the calorimeter. A 3.18 mm diameter stainless steel rod was used as the cathode. The cathode tip was a cone frustum with a 0.65 mm diameter top surface. The cathode was installed from the calorimeter base and secured in place by a Swagelok fitting. A

constant inter-electrode distance of 5.2 mm was maintained throughout for the present study.

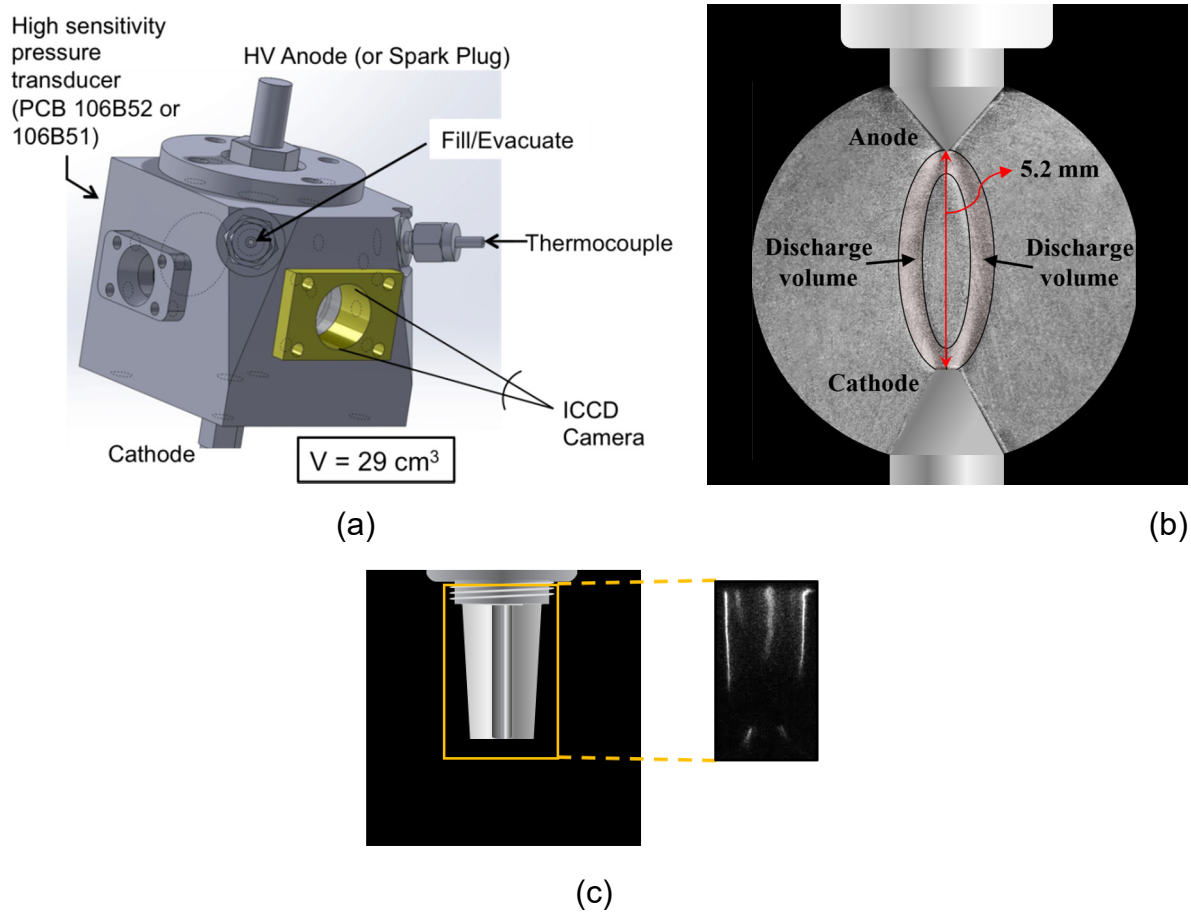

Figure 1: (a) 3D model of the optically accessible spark calorimeter. Electrode configuration and LTP discharge for (b) schematic of the pin-to-pin electrode with a complementary schlieren image of the discharge streamers, (c) schematic of the groundless partial DBD electrode and a complementary image of discharge excited state atomic oxygen.

A schematic of the groundless DBD electrode configuration is shown in Figure 1 (c). The electrode is a modified M12 Brisk silver center electrode non-resistor spark plug (MR12S) that has the J-hook removed and insulator tip exposed, with the anode ground flush to the surface of the ceramic.

Measured profiles of voltage, current, and integrated power for a 19.2 kV peak voltage discharge are presented in Figure 2. Only a fraction of the pulse energy was deposited into the gas as LTP, with the remainder reflected back and forth between the anode and the pulse generator. Voltage and current oscillations were damped by some combination of cable resistance and radiative emission, with little LTP energy addition after the first reflection as evidenced by the nearly invariant integrated power values after each reflection.

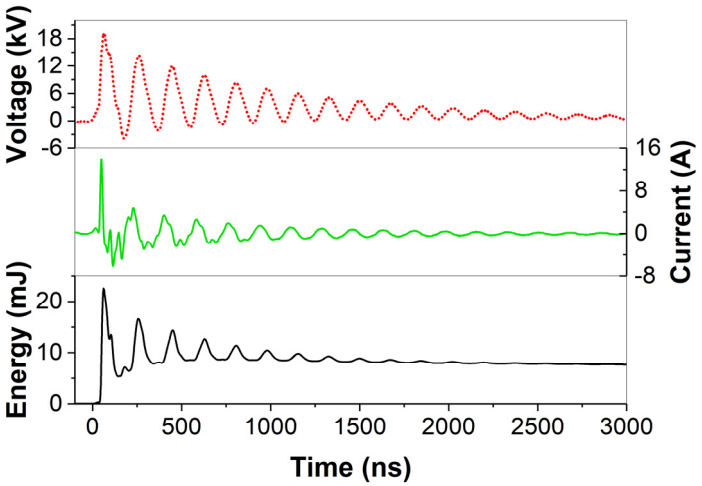

Figure 2: Instantaneous voltage, current, and integrated power in 20.95% O_2 at 70°C.

2.2. Experimental Conditions

Voltage and initial pressure conditions for the sampling and discharge imaging experiments are summarized for both electrode configurations in Table 2 and are plotted on the breakdown transition diagram in Figure 3.

Table 2: Experimental conditions.

		Initial pressure (bar)	
#	Voltage (kV)	Pin-to-pin	Partial DBD
1	10.3	1.2	–
2	14.4	1.5	1.5
3	14.4	2.1	–
4	19.2	2.1	3.0
5	22.5	–	4.5
6	25.0	–	6.1

For the pin-to-pin configuration, peak voltages were varied between 10.3 and 19.2 kV, while initial pressures were varied between 1.2 and 2.1 bar. For the groundless partial DBD electrode, a broader range of initial pressures (1.5 – 6.1 bar) and discharge voltages (14.4 – 25.0) was examined due to the lower propensity of the electrode to transition to breakdown. Experimental conditions were selected to investigate: (1) initial pressure variations with a fixed peak voltage, (2) variations in discharge voltage for a fixed pressure, and (3) discharge characteristics near the breakdown limit.

Also overlaid on the breakdown transition diagram for the pin-to-pin electrode (Figure 3a) is a plot of calculated breakdown voltage in air obtained from an empirical correlation developed by Pashley et al. [20]. For the current setup, the correlation underestimates breakdown voltages for initial pressures below 2.5 bar, possibly due to the truncated pulse that inhibits the time available for transition to breakdown. Conversely, the correlation overestimates breakdown voltages for higher initial pressures, likely due to the increased propensity for breakdown to occur during one of the reflected pulses described above rather than during the initial pulse. Nonetheless, there was good agreement between the correlation and measured breakdown.

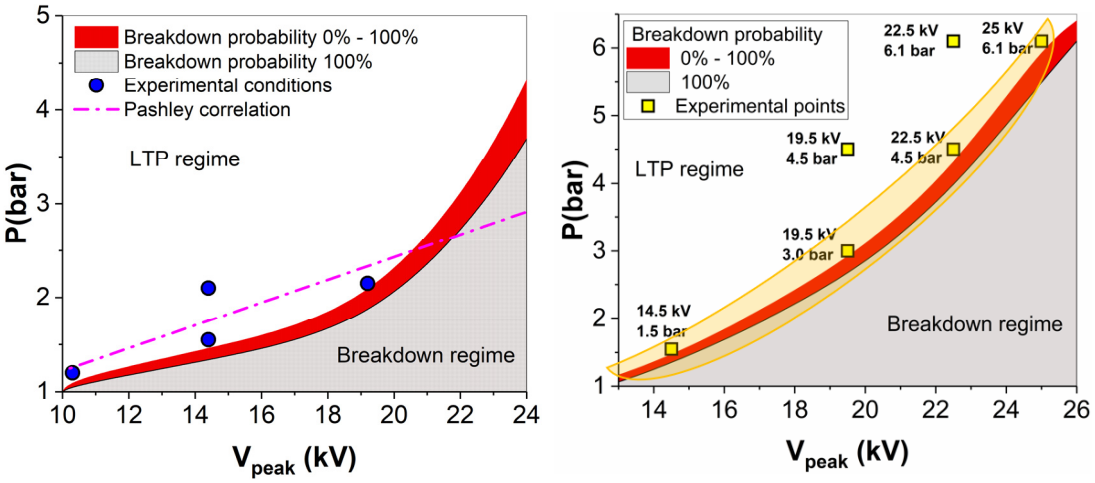

Figure 3: Experimental conditions for TPI.

2.3. Pressure-Rise Calorimetry

To estimate the globally averaged discharge temperature within the plasma streamer channels, pressure-rise calorimetry was performed in conjunction with schlieren imaging. The bulk-averaged thermal energy deposited into the calorimeter gas mixture, $E_{thermal}$ due to discharge is expressed as,

$$E_{thermal} = \int \Delta u d\mathbb{V} = \int \rho c_v \Delta T d\mathbb{V} = \frac{c_v}{R}\mathbb{V}\Delta P = \frac{\mathbb{V}\Delta P}{\gamma - 1} \quad (1)$$

where the variable u is the internal energy, $\mathbb{V}$ is the calorimeter volume, ρ is the gas density, c_v is the specific heat for air at constant volume, R is the gas constant, ΔT is the change in streamer gas temperature, ΔP is the change in calorimeter pressure, and γ is the air specific heat ratio. For each experimental condition, ΔP was calculated as the ensemble average of the peak pressure rise from 50 discharges. Due to the small ΔP encountered in the experiments, a constant γ (= 1.4) based on the initial gas temperature was assumed. To ensure that residual discharge products did not persist between runs and possibly influence the subsequent discharge, chamber contents after each run were cycle-purged twice using fill and vacuum solenoid valves connected to the gas supply and an available vacuum turbo-pump. Chamber fill pressure was accurately controlled using a Proportion-Air QPV pressure control valve. Differential chamber pressures were measured using a PCB 106B51 high-sensitivity pressure transducer (145 $\mu V/Pa$). The transducer was secured to the calorimeter using an acetal mounting adapter for electrical isolation with the signal amplified by a Kistler 5134B coupler. All data were recorded using a LeCroy HDO 6054 500 MHz high-definition oscilloscope. Recorded pressures were filtered by a 1 kHz low-pass filter during post-processing to remove noise from the discharge event.

2.4. Schlieren Imaging

Schlieren imaging was performed for each discharge using a pulsed green LED and a PI-MAX 4 camera operated at 10 μs exposure time; a schematic of the setup is shown

in Figure 4 (a). The camera was phase-locked with the discharge timing to record one image 1 μs after every discharge event. Schlieren images were post-processed to remove noise and increase contrast.

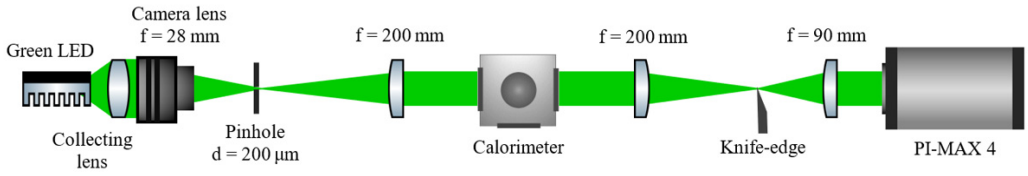

(a)

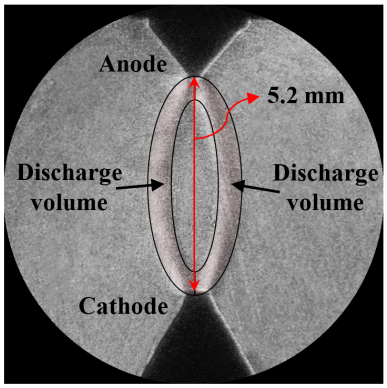

(b)

Figure 4: (a) Schematic of schlieren imaging to visualize the streamer discharges. (b) Identification of major schlieren image features for the pin-to-pin discharge.

For the pin-to-pin electrode, 2 dominant streamer channels were always observed in the schlieren images that connected the anode to the cathode, as illustrated in Figure 4 (b). The total streamer volume, $\mathcal{V}$, was estimated under the assumption that each branch was axisymmetric. Streamer channel edge detection in the schlieren image was determined by employing the Marr-Hildreth edge detection routine [21]. The spatially averaged translational temperature within the plasma streamer channel, T_{plasma}, was then calculated using $E_{thermal}$ and $\mathcal{V}$ as follows:

$$T_{plasma} = T_{initial} + \Delta T = T_{initial} + \frac{E_{thermal}}{\rho c_p \mathcal{V}} \quad (2)$$

Values for T_{plasma} estimated from Equations (1) and (2) are plotted in Figure 4 (c).

2.5. Post-discharge gas sampling and speciation

Post-discharge products from propane/air mixtures were acquired using a solenoid sampling valve that was connected the ignition test vessel to an evacuated and heated 0.5-liter sampling bottle. The equivalence ratio was maintained below the flammability limit to gain insight into the type and quantity of species generated from the transient plasma discharge. Sampling bottle hydrocarbon constituents were analyzed using an SRI Instruments Multi-Gas Analyzer gas chromatograph (GC) that contained a slow eluting 2-meter Restek Hayesep-N column, with hydrocarbon detection by a flame

ionization detector (FID). The column also contained a methanizer that enabled concurrent CO and CO_2 Measurements.

3. Numerical Model

3.1 Plasma discharge model

Only a general overview of the numerical modeling method is provided here; a more detailed description can be found in [22, 23]. Two-dimensional axisymmetric numerical simulations were performed using VizGlow – a general purpose self-consistent, multi-species, multi-temperature, non-equilibrium plasma solver that can be specialized to model high-pressure corona, glow or streamers discharge of interest [24]. Governing differential equations that account for the production, destruction, and transport of multiple charged and neutral species and the electron energy distribution are solved in conjunction with the Poisson's equation for the self-consistent electrostatic field. Photoionization, which is an important source of background electrons, is also accounted for.

Electrode surfaces are treated as equipotential surfaces for the electrostatic potential solution and as solid surfaces with wall boundary processes for the species density and temperature equations. A numerical grid consisting of a mixed triangle and quadrilateral cells is used for the simulations, with refined triangle cells used at the electrode surfaces to properly account for the electrode geometry so that the static electric field is properly predicted. The discharge voltage profile is matched to experimentally measured traces, with the minimum $2x10^{-13}$ s time step set such that the dynamics of the transient voltage discharge are well captured. A total of 150 ns simulation time includes the entire first pulse oscillation from the experiments when most electrical energy is deposited into the gas.

The air plasma chemical kinetic mechanism consists of 18 species: e, O_2, O_2*, O_2(a1), O_2(b1), O_2^+, O_2^-, O, O^-, O_4^+, O_2+N_2, N_2, N_2(a1), N_2(A), N_2(B), N_2(C), N_2^+, and N_4^+. The initial electron number, e, density is set at 10^3 cm^{-3}, which is also the default ground level for all considered species other than O_2 and N_2. Reaction rate pathways from the streamer plasma mechanisms were obtained from literature [25, 26], while electron impact reactions of O_2 and N_2 were generated offline using the Boltzmann solver BOLSIG+ [27] and cross-sectional data for N_2 and O_2 [25]. Energy lost to different rotational, vibrational, and electronic excitations combined into a single electron energy loss pathway.

3.2 0D CHEMKIN PRO flame speed and auto-ignition delay modeling

Discharge product concentrations from the sampling and gas chromatography results were used as input boundary conditions to model flame speeds and auto-ignition delays via CHEMKIN-PRO for stoichiometric mixtures. Based on complementary discharge imaging of excited state atomic oxygen, it was assumed that all discharge products constrained and homogeneously distributed within the 1 mm volume surrounding the electrode surface, with measured concentrations from the GC sampling results accordingly adjusted based on the ratio of the chamber volume to the assumed discharge volume.

4. Results and Discussions

Results are divided into three subsections. The first two sections respectively describe transient plasma discharge characteristics for the pin-to-pin and groundless DBD electrode configurations for nonflammable fuel/air discharges. The third subsection discusses TPI characteristics for stoichiometric mixtures of propane and desiccated air.

4.1 Discharge Characteristics: Pin-to-pin Electrode Configuration

As mentioned in the Experimental Approach, the pin-to-pin electrode configuration was selected for examination because it produces strong local field concentrations at both the anode and cathode tips. As a result, radical generation favorable for ignition promotion along with increased temperature from the relaxation of vibrationally and electronically excited species are both expected to be high in these regions.

The schlieren image in Figure 5 was acquired shortly after a 19.2 kV discharge into a 2.0 bar ambient of air. The discharge led to the formation of twin streamers that joined at the anode and cathode but separated near the midpoint of the electrode gap. Note that the orientation of streamers changes randomly. The image in Figure 5 was the image from a set of 50 images that had the streamer channels were most closely oriented orthogonal to the camera and thus best illustrates the streamer features. Complementary numerical simulations likewise predict the appearance of twin streamers, with maximum concentrations of atomic oxygen and electron density predicted to occur near the anode. The location of maximum atomic oxygen generation is strongly dependent on the local electric field which in turn is a function of the electrode geometry. Table 3 compares the temperature and atomic oxygen number density from experiment and numerical simulations.

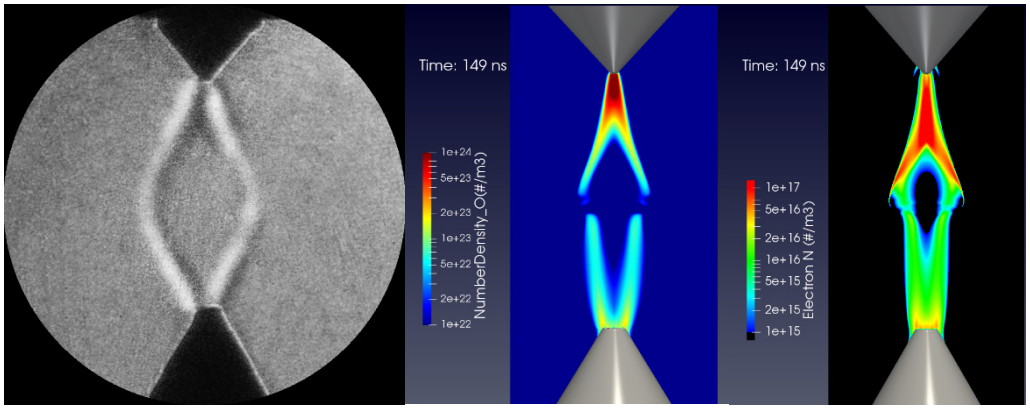

Figure 5: Post-discharge schlieren image from a 19.2 kV transient plasma discharge in 2.0 bar of air along with complementary VizGlow simulation predictions of atomic oxygen and electron density distributions.

Table 3: Comparison of discharge characteristics in terms of LTP temperature and atomic oxygen number density from experiments and numerical simulation.

Experimental condition	**Simulations**		**Experiments**	
	O (#/m^3)	T (K)	O (#/m^3)	T (K)
14kV - 1.5bar	0.9E^{+24}	770	1.3E^{+24}	779
19kV - 2.0bar	1.8E^{+24}	938	2.1E^{+24}	1094

Similar images were acquired at different initial pressure and peak discharge voltage combinations (not shown). In all instances, the peak streamer separation distance slightly biased toward the lower cathode. Moreover, as the discharge voltage increased, the separation distance between each streamer likewise increased.

In Figure 6, discharge energy (measured by an in-line voltage and current probe) as a function of peak discharge voltage is plotted along with the corresponding energy deposited into the gas (measured from the pressure-rise calorimetry). The plot also includes an estimate of the bulk-averaged streamer temperature acquired from the combined calorimetry and schlieren measurements described earlier. As expected, the total discharge energy is proportional to the peak discharge voltage. However, the fraction of energy deposited into the gas increases with higher discharge energies, which results in a non-linear increase in streamer temperature. Note for the peak discharge voltage of 19.2 kV; the average streamer temperature was measured for three different initial pressures (2.0, 2.5, and 3.0 bar). As can be seen in Figure 6, streamer temperatures were virtually identical due to the fact that streamer volume was inversely proportional to initial pressure.

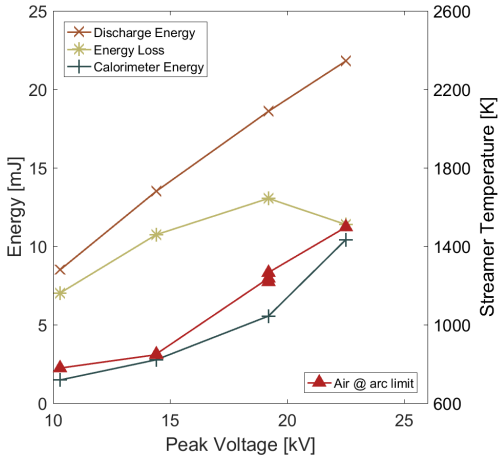

Figure 6: Measured discharge, energy deposition into the gas, energy lost from the system, and the estimated mean streamer temperature.

Since translational temperature is perhaps the most important parameter for ignition, there is a clear advantage to higher discharge voltages. However, for small gaps or low ambient densities the discharge transitions to breakdown.

Finally, note that sampling of non-flammable discharge products was performed for the pin-to-pin configuration, but no measurable concentrations of discharge products were obtained regardless of the condition. Despite the elevated electric fields within the

vicinity of the anode, the small volumes around the electrode tips led to the negligible generation of active radicals on a global scale.

4.2 Discharge Characteristics: Groundless partial DBD Electrode Configuration

The groundless partial DBD electrode was selected because it was assumed to be more resistant to breakdown transition. In addition, a larger discharge volume is preferential for lean/dilute charge mixtures where ignition is more challenging. LTP discharge characteristics from the groundless partial DBD electrode are shown in Figure 7 for discharges with peak voltages near the breakdown limit for the respective initial pressure. Discharge characteristics shows that the streamers start from the remaining portion of the spark plug ground and vertically extend toward the anode. The streamer length and luminescence increased with increased discharge voltage and initial pressure. However, the location of the streamers in successive discharge is stochastic. The expectation is that each streamer acts as both a local ignition site and enhances initial flame burn rates due to the favorable radical formation. Tests of these hypotheses will be described in the following section.

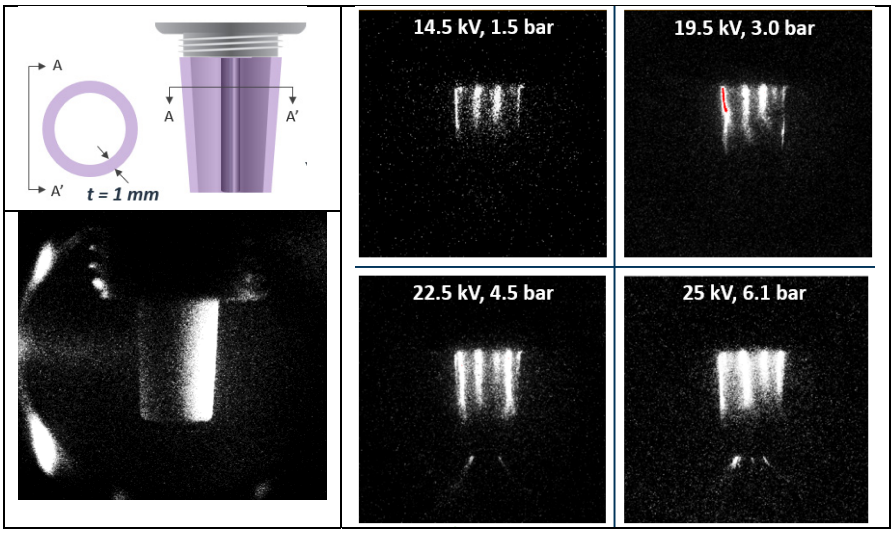

Figure 7: Schematic of the groundless partial DBD electrode including the assumed discharge active area, and qualitative images of O.*

For post-discharge product sampling, discharges were performed in propane/air mixtures. The 2% propane concentration was below the lean flammability limit. To generate statistically meaningful post-discharge products, 10 discharges, 10 milliseconds apart was repeated 60 times.

Figure 8 plots the speciated post-discharge products formed from the LTP discharges, where the initial pressure was adjusted so that breakdown was avoided for the respective discharge voltage. Several hydrocarbon products with carbon numbers less than 3 were formed, which include: methane, CO, acetylene, ethylene, propylene, cyclopropane, acetone. Methane, acetylene, CO, and cyclopropane concentrations, in

particular, were found to increase substantially with higher peak voltages, while remaining species concentrations were relatively stable.

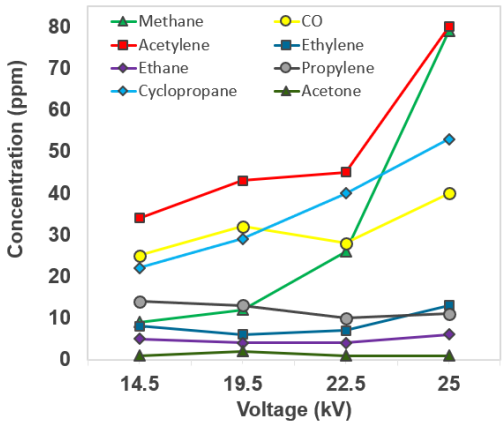

Figure 8: GC measurement of post LTP discharge species formed by groundless DBD electrode discharges.

The effect of initial pressure for a fixed discharge voltage and discharge voltage for a fixed initial pressure on post-discharge product formation is shown in Figure 9. For the ambient pressure variation, most species concentrations were unchanged except for CO and acetylene, which decreased substantially when the initial pressure was increased. When peak voltage was changed for a fixed initial pressure, all discharge products increased; with increases for acetone, cyclopropane, methane, and CO being the most pronounced.

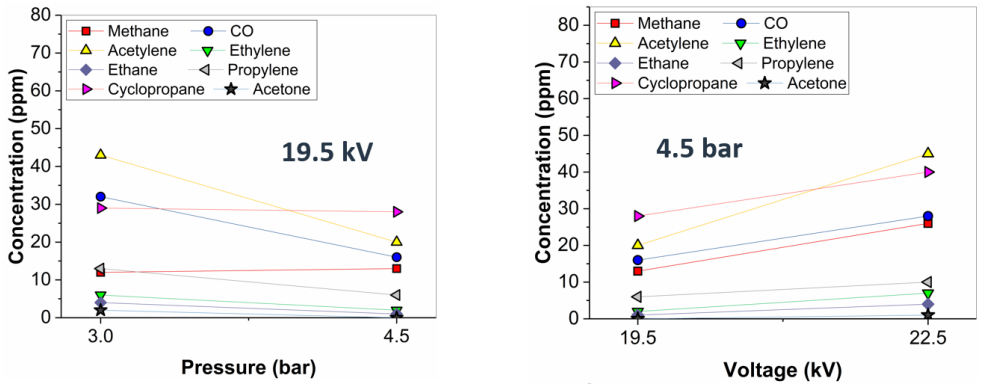

(a) (b)

Figure 9: The effect of (a) pressure, (b) voltage on post-discharge product formation.

To explore the effect of post-discharge products on charge reactivity, CHEMKIN PRO simulations were performed. Discharge product concentrations from the condition with 19.2 kV peak voltage and 2.0 bar initial pressure were used, with the balance of fuel set to be the parent propane mixture. Table 4 shows the volume percentage of LTP products and additional propane/air concentration.

Table 4: Volume percentage of mixture components used in the CHEMKIN PRO model.

% by Vol.	LTP products + propane/air	Propane/air
O_2	20.2	20.2
N_2	75.8	75.8
Propane	2.5	4
Methane	0.26	
CO	0.22	
Acetylene	0.51	
Ethylene	0.1	
Propylene	0.12	
Cyclopropane	0.26	
Acetone	0.03	

In Figure 10, flame speed and ignition delay predictions from the CHEMKIN modeling are compared with an equivalent equivalence ratio of propane/air mixture. Figure 10 (a) shows that with increased pressure, ignition delays decreased in the presence of post-discharge products by up to 20%, which suggests that the mixture becomes more reactive. Conversely, Figure 10 (b) shows that flame speeds increased in the presence of discharge products by up to 20%, which suggests faster initial ignition kernel growth rates can be expected.

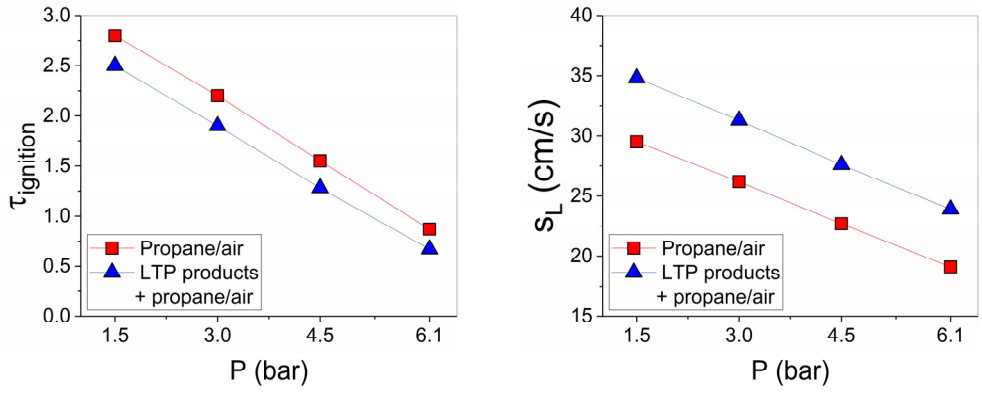

Figure 10: The effect of post-discharge products on (a) ignition delay, (b) laminar flame speed.

4.3 Transient Plasma Ignition Flame Propagation Characteristics

Schlieren image sequences of ignition kernel development and subsequent flame propagation at discrete times after the discharge are plotted in Figure 11 for the pin-to-pin and groundless partial DBD electrodes, along with a comparison to ignition form a high-energy (93 mJ) inductor coil spark plug igniter. The fuel was propane, while the oxidizer was desiccated air. Concentrations were fixed at stoichiometric conditions (6.45% propane in air). The initial pressure was 1.3 bar absolute. Pulse bursts of 5 and 10 pulses were examined for TPI (ignition was not achieved for a 5 pulse burst for either TPI igniter at the conditions examined). In all cases, the dwell between successive pulses was 100 μs. Peak voltage and pulse number are tabulated at the end of the respective sequence. Note that for the groundless partial DBD electrode,

two sets of images were acquired: (1) electrode tip in view to examine ignition processes along the insulator, and (2) electrode tip at the upper edge of the image to examine flame propagation processes in detail.

The ignition location of TPI is key information that helps combustion system developers design optimal electrodes. For the pin-to-pin configuration, ignition was achieved for a peak pulse voltage of 15 kV and pulse burst of 10. Ignition initiated at both the cathode and anode, and quickly bridged the gap following one of the two discharge streamers. For the groundless DBD electrode, the peak voltage needed to be increased to 24 kV for ignition to occur. Ignition started at the exposed anode tip, with a hemispherical laminar flame front developing shortly thereafter. Initially, this flame front propagated outward from the tip, but quickly moved up along the DBD surface.

For both TPI electrodes, the resultant flames kernels consumed the field of view within 3.0 milliseconds after the start of the discharge, whereas the flame from the inductor coil igniter had consumed only half of this area by the same time. From the image sequences, the flame front location was estimated as a function of time after the discharge and plotted in Figure 12. These profiles again illustrate that TPI flame propagation rates were roughly double compared to the discharge from the inductor coil spark plug, with very little difference observed for the pin-to-pin and groundless partial DBD ignition.

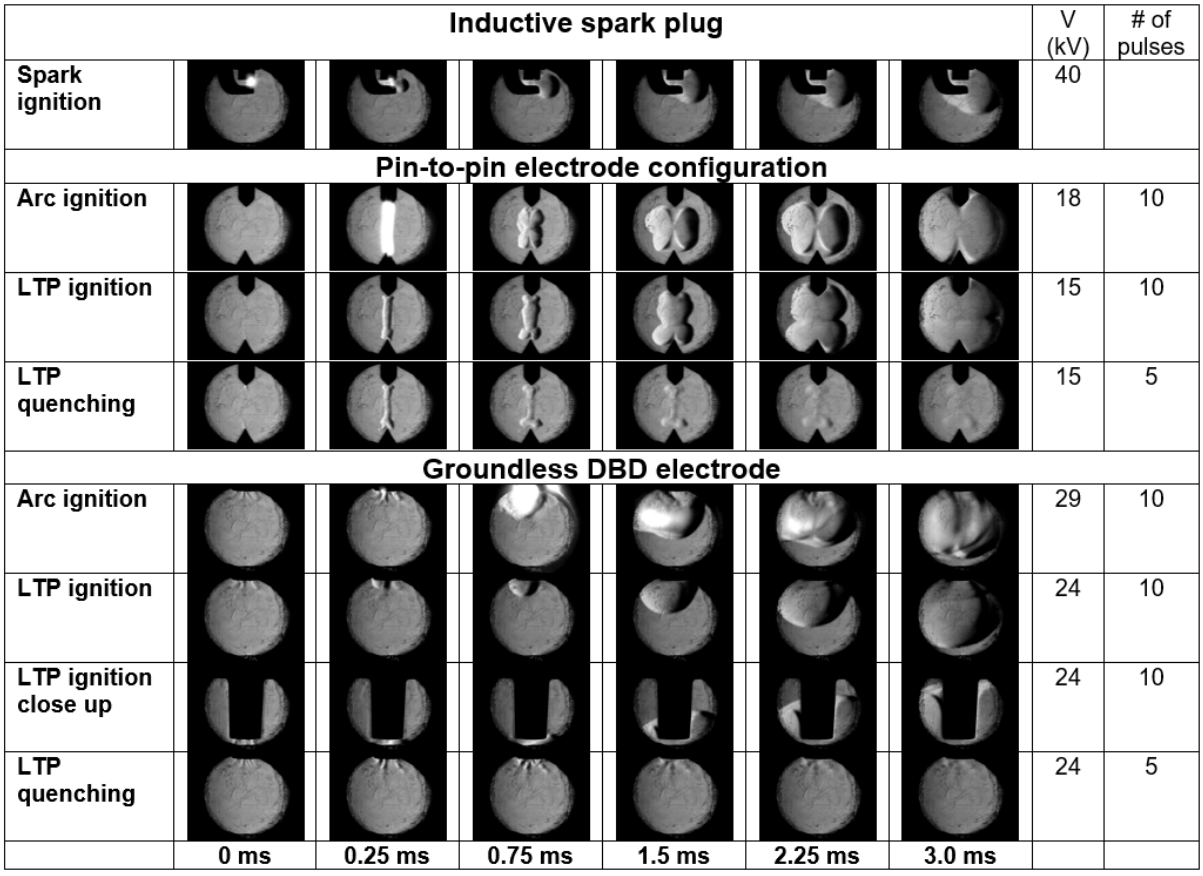

Figure 11: Sequence of images showing ignition kernel development in TPI compared to inductive spark for different voltage and pulse repetition rate.

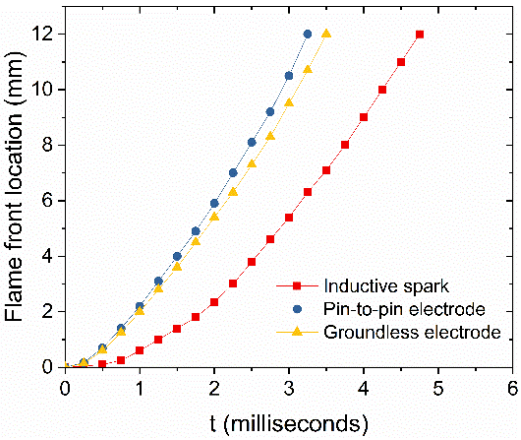

Figure 12: Time history of flame front displacement in TPI and spark ignition.

Note that the while both TPI systems performed similarly, the groundless partial DBD igniter was much more resistant to electrical breakdown. Figure 11 illustrates sequences characterized by breakdown or arcing events. In each instance, highly luminous discharges are visible within the within the first millisecond after the first discharge. The breakdown voltages were only 3 kV higher for the pin-to-pin electrode, whereas they were 5 kV higher for the groundless partial DBD electrode. Accordingly, the DBD electrode is slightly more forgiving, although it comes at the cost of higher energy draw.

5. Conclusions

The present paper discusses the characteristics of nanosecond transient plasma and TPI in an optically accessible, spark calorimeter at gasoline engine relevant densities. Major findings are as follows:

- Discharge characteristics from pin-to-pin show that the existence of twin streamers that bridge the electrode gap. Complementary plasma modeling simulations illustrate that peak atomic oxygen number and electron densities occur near the anode. Post-discharge streamer temperatures increase with higher discharge voltages, likely due to higher energization of vibrational and electronic states that subsequently relax and form heat.
- For groundless partial DBD electrode, multiple negative corona streamers initiate from the remaining ground thread and extend towards the anode. Bulk-sampling with speciation via GC indicates extensive dissociation of the parent fuel molecule into smaller hydrocarbon components. Complementary flame speed modeling that uses these concentrations as an initial condition indicate increased flame speeds of up to 20%. Accordingly, these post-discharge products may play a vital role in flame kernel development rates.
- For both TPI electrodes, a 10-pulse burst (at 10 kHz) was required to achieve sustainable ignition kernel development, with fewer pulses leading to the gradual extinction of the developed kernel. These results suggest the energy within the kernel must be systematically replenished in order to sustain ignition in the earliest phases.
- The pin-to-pin TPI electrode initiates ignition at both the anode and cathode, with the initial flame kernel quickly propagating up along one or both of the discharge streamers that result from the discharge. The groundless partial DBD

electrode initiated ignition at the electrode tip, with combustion propagating outward into the bulk gas and quickly up along the insulator surface.
- Relative to a conventional inductor coil ignition system (93 mJ), both TPI igniters roughly doubled the flame propagation rates.
- Larger discharge voltages were needed to initiate TPI with the groundless partial DBD electrode relative to the pin-to-pin configuration (24 vs. 15 kV). However, the groundless partial DBD electrode was much less prone to arc due to the design that shielded the anode from the propagating negative corona streamers. Thus, despite the higher energy draw, the groundless DBD electrode likely is a more robust design.

Future work will explore the possible extension of these TPI electrodes to lean and dilute conditions. Moreover, the ability of these electrodes to promote ignition at pressures and temperatures relevant to those within a realistic engine chamber will be investigated. These results will be complemented by detailed plasma dynamics and computational fluid dynamic simulations that attempt to capture all relevant processes.

Acknowledgments

The work was performed at the Combustion Research Facility, Sandia National Laboratories, Livermore, CA. Financial support was provided by the U.S. Department of Energy, Vehicle Technologies Office. Sandia National Laboratories is a multi-mission laboratory managed and operated by National Technology and Engineering Solutions of Sandia, LLC., a wholly owned subsidiary of Honeywell International, Inc., for the U.S. Department of Energy's National Nuclear Security Administration under contract DE-NA0003525. This paper describes objective technical results and analysis. Any subjective views or opinions that might be expressed in the paper do not necessarily represent the views of the U.S. Department of Energy or the United States Government. The authors also gratefully acknowledge the engineering support provided by Alberto Garcia and Keith Penney, fruitful technical discussions with Caroline Winters, Bo Zhou, and Joonsik Hwang of Sandia National Laboratories and hardware support by Daniel Singleton and Jason Sanders of Transient Plasma Systems Inc.

References

1. Dunn-Rankin, D., "*Lean combustion : technology and control*. 2008, Amsterdam; Boston: Academic Press. xi, 261 p., 8 p. of plates.
2. Rapp, V., N. Killingsworth, P. Therkelsen, and R. Evans, "*Lean-Burn Internal Combustion Engines,*" 2016: p. 111-146.
3. Dale, J.D., M.D. Checkel, and P.R. Smy, "*Application of high energy ignition systems to engines,*" Progress in Energy and Combustion Science, 1997. 23(5-6): p. 379-398.
4. Nishiyama, A. and Y. Ikeda, "*Improvement of Lean Limit and Fuel Consumption Using Microwave Plasma Ignition Technology,*" SAE International Technical Paper, 2012. 2012-01-1139.
5. Michael, J.B., T.L. Chng, and R.B. Miles, "*Sustained propagation of ultra-lean methane/air flames with pulsed microwave energy deposition,*" Combustion and Flame, 2013. 160(4): p. 796-807.

6. Leonov, S.B. and D.A. Yarantsev, "*Plasma-induced ignition and plasma-assisted combustion in high-speed flow,*" Plasma Sources Science and Technology, 2007. 16(1): p. 132-138.
7. Chintala, N., A.N. Bao, G.F. Lou, and I.V. Adamovich, "*Measurements of combustion efficiency in nonequilibrium RF plasma-ignited flows,*" Combustion and Flame, 2006. 144(4): p. 744-756.
8. Bozhenkov, S.A., S.M. Starikovskaia, and A.Y. Starikovskii, "*Nanosecond gas discharge ignition of H 2 − and CH 4 − containing mixtures,*" Combustion and Flame, 2003. 133(1): p. 133-146.
9. Kosarev, I.N., N.L. Aleksandrov, S.V. Kindysheva, S.M. Starikovskaia, and A.Y. Starikovskii, "*Kinetic mechanism of plasma-assisted ignition of hydrocarbons,*" Journal of Physics D: Applied Physics, 2008. 41(3).
10. Starikovskiy, A. and N.L. Aleksandrov, "*Plasma-assisted ignition and combustion,*" Progress in Energy and Combustion Science, 2013. 39(1): p. 61-110.
11. Sjöberg, M., W. Zeng, D. Singleton, J.M. Sanders, and M.A. Gundersen, "*Combined Effects of Multi-Pulse Transient Plasma Ignition and Intake Heating on Lean Limits of Well-Mixed E85 DISI Engine Operation,*" SAE International Journal of Engines, 2014. 7(4): p. 1781-801.
12. Sevik, J., T. Wallner, M. Pamminger, R. Scarcelli, D. Singleton, and J. Sanders, "*Extending Lean and Exhaust Gas Recirculation-Dilute Operating Limits of a Modern Gasoline Direct-Injection Engine Using a Low-Energy Transient Plasma Ignition System,*" Journal of Engineering for Gas Turbines and Power, 2016. 138(11): p. 1-9.
13. Sun, W., M. Uddi, S.H. Won, T. Ombrello, C. Carter, and Y. Ju, "*Kinetic effects of non-equilibrium plasma-assisted methane oxidation on diffusion flame extinction limits,*" Combustion and Flame, 2012. 159(1): p. 221-230.
14. Wolk, B., A. DeFilippo, J.Y. Chen, R. Dibble, A. Nishiyama, and Y. Ikeda, "*Enhancement of flame development by microwave-assisted spark ignition in constant volume combustion chamber,*" Combustion and Flame, 2013. 160(7): p. 1225-1235.
15. Mintusov, E., A. Serdyuchenko, I. Choi, W.R. Lempert, and I.V. Adamovich, "*Mechanism of plasma assisted oxidation and ignition of ethylene–air flows by a repetitively pulsed nanosecond discharge,*" Proceedings of the Combustion Institute, 2009. 32(2): p. 3181-3188.
16. Kosarev, I.N., N.L. Aleksandrov, S.V. Kindysheva, S.M. Starikovskaia, and A.Y. Starikovskii, "*Kinetics of ignition of saturated hydrocarbons by nonequilibrium plasma: CH_4-containing mixtures,*" Combustion and Flame, 2008. 154(3).
17. Cathey, C., J. Cain, H. Wang, and M.A. Gundersen, "*OH production by transient plasma and mechanism of flame ignition and propagation in quiescent methane-air mixtures,*" Combustion and Flame, 2008. 154(4).
18. Singleton, D., S.J. Pendleton, and M.A. Gundersen, "*The role of non-thermal transient plasma for enhanced flame ignition in C2H4-air,*" Journal of Physics D: Applied Physics 2011. 44(2): p. 022001-22002.
19. Wolk, B. and I. Ekoto, "*Calorimetry and Imaging of Plasma Produced by a Pulsed Nanosecond Discharge Igniter in EGR Gases at Engine-Relevant Densities,*" SAE International Journal of Engines, 2017. 10(3).
20. Pashley, N., R. Stone, and G. Roberts, "*Ignition System Measurement Techniques and Correlations for Breakdown and Arc Voltages and Currents,*" SAE Technical Paper 2000-01-0245, 2000.

21. Marr, D. and E. Hildreth, "*Theory of Edge Detection,*" Proceedings of the Royal Society of London. Series B, Biological Sciences, 1980. 207(1167): p. 187-217.
22. Scarcelli, R., A. Zhang, and T. Wallner, "*Multi-dimensional modeling of non-equilibrium plasma for automotive applications,*" SAE Technical Paper 2018-01-0198, 2018.
23. Zhang, A., R. Scarcelli, T. Wallner, D. Breden, A. Karpatne, L.L. Raja, I. Ekoto, and B. Wolk, "*Numerical investigation of nanosecond pulsed discharge in air at above-atmospheric pressures,*" Journal of Physics D: Applied Physics, 2018. 51(34).
24. VizGlow. *http://esgeetech.com/*.
25. Kossyi, I.A., A.Y. Kostinsky, A.A. Matveyev, and V.P. Silakov, "*Kinetic scheme of the non-equilibrium discharge in nitrogen-oxygen mixtures,*" Plasma Sources Science and Technology, 1992. 1(3): p. 207-220.
26. Pancheshnyi, S., M. Nudnova, and A.Y. Starikovskii, "*Development of a cathode-directed streamer discharge in air at different pressures: Experiment and comparison with direct numerical simulation,*" Physical Review. E, Statistical, Nonlinear, And Soft Matter Physics, 2005. 71(1).
27. Hagelaar, G.J.M. and L.C. Pitchford, "*Solving the boltzmann equation to obtain electron transport coefficients and rate coefficients for fluid models,*" Plasma Sources Science and Technology, 2005. 14(4): p. 722-733.